



# Finite element investigation into the use of carbon fibre reinforced PEEK laminated composites for distal radius fracture fixation implants

Elizabeth Anne Gallagher<sup>a</sup>, Steven Lamorinière<sup>b</sup>, Patrick McGarry<sup>a,\*</sup>

<sup>a</sup> Biomedical Engineering, National University of Ireland Galway, University Road, Galway, Ireland

<sup>b</sup> Invibio Ltd., Hillhouse International, Thornton-Cleveleys FY5 4QD, United Kingdom

## ARTICLE INFO

### Article history:

Received 18 October 2018

Revised 25 February 2019

Accepted 3 March 2019

Available online xxx

## ABSTRACT

Carbon fibre reinforced PEEK (CF/PEEK) laminates provide mechanical advantages over homogenous metal osteo-synthesis implants, e.g. radiolucency, fatigue strength and strength to weight ratio. Implants can be designed with custom anisotropic material properties, thus enabling the engineer to tailor the overall stiffness of the implant to the specific loading conditions it will experience *in vivo*.

In the current study a multi-scale computational investigation of idealised distal radius fracture fixation plate (DRP) is conducted. Physiological loading conditions are applied to macro-scale finite element models of DRPs. The mechanical response is compared for several CF/PEEK laminate layups to examine the effect of ply layup design. The importance of ply orientation in laminated DRPs is highlighted. A high number of 0° plies near the outer surfaces results in a greater bending strength while the addition of 45° plies increases the torsional strength of the laminates. Intra-laminar transverse tensile failure is predicted as the primary mode of failure.

A micro-mechanical analysis of the CF/PEEK microstructure uncovers the precise mechanism underlying intra-laminar transverse tensile crack to be debonding of the PEEK matrix from carbon fibres. Plastic strains in the matrix material are not sufficiently high to result in ductile failure of the matrix. The findings of this study demonstrate the significant challenge in the design and optimisation of fibre reinforced laminated composites for orthopaedic applications, highlighting the importance of multi-scale modelling for identification of failure mechanisms.

© 2019 IPEM. Published by Elsevier Ltd. All rights reserved.

## 1. Introduction

The stiffness of metallic orthopaedic implants, e.g. femoral stems or fracture fixation plates, is an order of magnitude greater than the stiffness of cortical bone. Furthermore, metal implants can cause problematic artefacts when subjected to MRI, CT and X-Ray imaging, resulting in a range of clinical complications in terms of correctly positioning the device and post-operative assessment [1]. A limited number of orthopaedic implants (e.g. vertebral cages used for spinal fusion) manufactured from short unaligned fibre reinforced poly-ether-ether-ketone (PEEK) have been investigated [2–5]. However, to date, very few continuous carbon fibre reinforced composite laminates (with multiple ply orientations) have been used for orthopaedic applications (CarboFix Orthopaedics Ltd.). Such laminated composites exhibit a high fatigue life and a high strength to weight ratio. They do not cause problematic artefacts when subjected to MRI, CT and X-Ray imaging

and have anisotropic material properties that can be tailored simply by altering the layup of the angled plies in the laminate. A continuous carbon fibre reinforced PEEK composite material, PEEK-OPTIMA™ Ultra-Reinforced (Invibio Ltd., Thornton-Cleveleys, UK) hereafter referred to as CF/PEEK, has been cleared for implantation in humans by the FDA. This study will investigate the use of CF/PEEK laminates for fracture fixation plates, highlighting the requirement of multi-scale finite element modelling for identification of optimal ply layups and failure mechanisms.

The first part of this study entails a macro-scale analysis of CF/PEEK distal radius fracture fixation plates (DRP). All material properties and material damage and failure parameters are based on the recent multi-axial experimental characterisation of CF/PEEK by Gallagher et al. [6]. Several layup designs are considered, and the mechanical performance of each design is computed under physiological loading conditions. In the second part of this study, multi-axial strain states, computed using the macro-scale DRP model, are applied to representative volume elements (RVEs) of the ply microstructure to obtain a new insight into the mechanisms of intra-ply failure. This study provides the first multi-scale analysis framework for CF/PEEK orthopaedic devices.

\* Corresponding author.

E-mail address: [patrick.mcgarry@nuigalway.ie](mailto:patrick.mcgarry@nuigalway.ie) (P. McGarry).

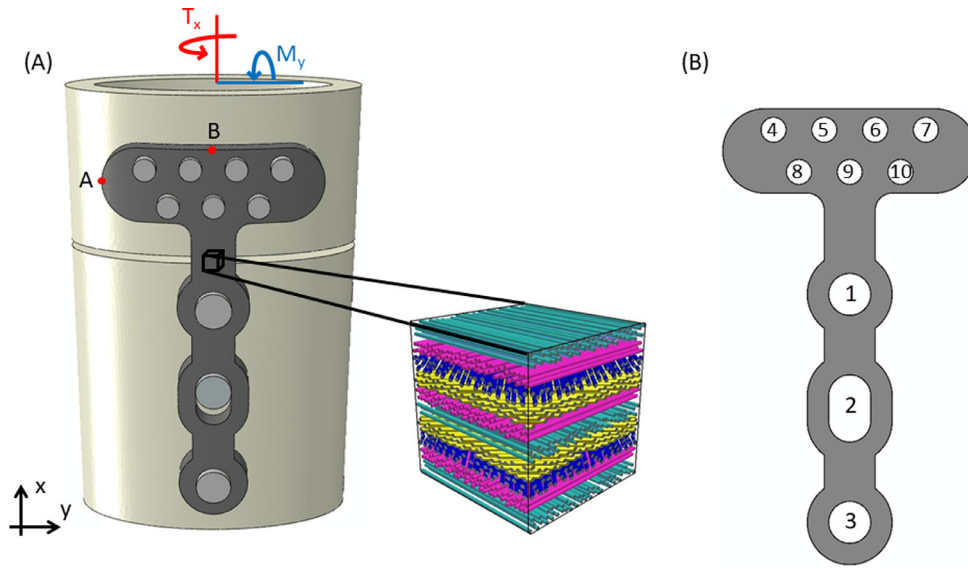


**Fig. 1.** (A) Generic distal radius fracture plate geometry attached to an idealised model of a fractured distal radius. A schematic of a 3D ply layup is included for illustrative purposes (ratio of fibre diameter to ply thickness is not to scale). Boundary conditions applied to distal radius are shown. (B) Illustration of the numbering used to identify specific holes in the DRP.

## 2. Model development

The multi-scale modelling approach implemented in the current study entails: (i) the analysis of the stress-strain distribution in the macroscopic composite distal radius fracture plates under physiological loading; (ii) analysis of intra-ply micro-structural failure mechanisms.

### 2.1. Macro-scale model of distal radius fracture plate

A generic geometry of a distal radius fracture fixation plate is created based on commercially available compression type implants [7]. The fixation plate is modelled in Abaqus 2017 (SIMULIA, Providence, RI, USA) using approx. 100,000 3D continuum elements (C3D8R). The plate is attached to an idealised bone

et al. [6]. In addition to comparing the performance of the laminate designs above, a homogeneous and isotropic titanium plate is simulated (Table 1).

### 2.2. Laminate computational damage and failure model

Fibre reinforced composite materials can exhibit a number of damage and failure mechanisms, which depend on the mode of loading. Damage mechanisms reported by Gallagher et al. for CF/PEEK include anisotropic plasticity, intra-laminar crack propagation and inter-laminar delamination [6]. The calibrated and validated damage and failure model for CF/PEEK developed by Gallagher et al. is used to analyse the performance of the composite implants described in Section 2.1.

The anisotropic yield behaviour of the laminate is computed using Hill's potential function [11].

$$f(\sigma) = \left( \sqrt{F(\sigma_{22} - \sigma_{33})^2 + G(\sigma_{33} - \sigma_{11})^2 + H(\sigma_{11} - \sigma_{22})^2 + 2L\sigma_{23}^2 + 2M\sigma_{31}^2 + 2N\sigma_{12}^2} \right) - \sigma_{yield} = 0 \quad (1)$$

geometry through rigid screw fixations at each screw hole. Boundary conditions that replicate the loading conditions induced during physiological movements of the wrist are applied to the plated bone. Unless otherwise stated physiological loading conditions will be torsion and bending moments of  $T_x = 0.68$  Nm and  $M_y = 1.05$  Nm [8–10], respectively (Fig. 1).

To assess the design requirements of the implant and determine the optimum ply layup, five laminate layup configurations are considered:

- Laminate 1: A unidirectional  $0^\circ$  CF/PEEK laminate  $[0_8]_s$ , hereafter referred to as ' $0^\circ$  laminate';
- Laminate 2: A unidirectional  $90^\circ$  CF/PEEK laminate  $[90_8]_s$ , hereafter referred to as ' $90^\circ$  laminate';
- Laminate 3: A CF/PEEK  $[\pm 45]_4s$  laminate, hereafter referred to as the ' $45^\circ$  laminate';
- Laminate 4: A CF/PEEK laminate with a ply layup of  $[\pm 45_2/0_4]_s$ ;
- Laminate 5: A  $[0_2/\pm 45]_2s$  CF/PEEK laminate.

All laminates have an equal number of plies (16), each ply has a thickness of 0.2 mm, and the fixation plates have an overall thickness of 3.2 mm. The material properties for a unidirectional CF/PEEK ply are outlined in Table 1 based on the study of Gallagher

where  $F$ ,  $G$ ,  $H$ ,  $L$ ,  $M$ , and  $N$  are constants obtained from experimental testing of the material. The anisotropic yield stress ratios  $R_{ij}$  calibrated from the experimental results of Gallagher et al. are listed in Table 1.

The intra-laminar failure criteria are based on a modified Hashin-type damage model, describing tensile and compressive crack formation in both the transverse and fibre directions within a ply, as described in Eqs. (2)–(5) below.

$$f_T^m = \left( \frac{(\sigma_{22} + \sigma_{33})^2}{Y_T^2} \right) + \left( \frac{\sigma_{23}^2 - \sigma_{22}\sigma_{33}}{S^2} \right) + \left( \frac{\sigma_{12}^2 - \sigma_{13}^2}{S^2} \right) \quad (2)$$

$$f_C^m = \left[ \left( \frac{Y_C}{2S_{23}} \right)^2 - 1 \right] \left( \frac{\sigma_{22} + \sigma_{33}}{Y_C} \right) + \frac{(\sigma_{22} + \sigma_{33})^2}{4S^2} + \frac{\sigma_{23}^2 - \sigma_{22}\sigma_{33}}{S^2} + \frac{\sigma_{12}^2 + \sigma_{13}^2}{S^2} \quad (3)$$

$$f_T^f = \left( \frac{\sigma_{11}}{X_T} \right)^2 + \left( \frac{\sigma_{12}}{S} \right)^2 + \left( \frac{\sigma_{13}}{S} \right)^2 \quad (4)$$

$$f_C^f = \left( \frac{\sigma_{11}}{X_C} \right)^2 + \left( \frac{\sigma_{12}}{S} \right)^2 + \left( \frac{\sigma_{13}}{S} \right)^2 \quad (5)$$

**Table 1**

Elastic material properties and tensile, compressive and shear strengths, inter-laminar CZM model parameters and anisotropic plasticity model parameters for macro-scale DRP simulations. Material properties for simulation of titanium DRP also presented.

CF/PEEK [6]			Titanium [15]		
$E_{11} = 175.4$ GPa	$X_T = 2882$ MPa	$\sigma_y = 111$ MPa	$\sigma_{max} = 49.5$ MPa	$E = 112$ GPa	
$E_{22} = 9.4$ GPa	$Y_T = 50$ MPa	$R_{11} = 250$	$\tau_{max} = 37$ MPa	$\nu = 0.3$	
$E_{33} = 9.4$ GPa	$X_C = 1182$ MPa	$R_{22} = 1.0$	$\delta_n = 10$ $\mu\text{m}$	$\sigma_y = 847$ MPa	
$\nu_{12} = 0.38$	$Y_C = 186$ MPa	$R_{33} = 1.0$	$\delta_t = 10$ $\mu\text{m}$		
$\nu_{13} = 0.38$	$S = 96$ MPa	$R_{12} = 0.64$			
$\nu_{23} = 0.46$	$G_{ic} = 1.44$ kJ/m <sup>2</sup>	$R_{13} = 0.64$			
$G_{12} = 5.2$ GPa	$G_{iic} = 1.0$ kJ/m <sup>2</sup>	$R_{23} = 1.0$			
$G_{13} = 5.2$ GPa					
$G_{23} = 1.9$ GPa					

where  $f_T^m$  and  $f_C^m$  are the tensile and compressive matrix failure criteria, respectively.  $f_T^f$  and  $f_C^f$  are the tensile and compressive fibre failure criteria, respectively.  $Y_T$  and  $Y_C$  are the transverse tensile and compressive strengths, respectively.  $X_T$  and  $X_C$  are the longitudinal tensile and compressive strengths, respectively, and  $S$  is the shear strength of the CF/PEEK material. When any of the above failure criteria equals 1 a crack is initiated. The extended finite element method (XFEM) [12] is implemented to simulate crack propagation through the laminate following initiation. The intra-laminar failure criteria are implemented through a user defined damage initiation subroutine (UDMGINI).

Inter-laminar failure, simulated using a cohesive zone formulation, is governed by the mode dependent traction separation relations defined below, developed by McGarry et al. [13]. The coupled dependence of interface traction on normal ( $\Delta_n$ ) and tangential ( $\Delta_t$ ) interface separation is described in Eqs. (6) and (7). A number example problems are presented in O'Mairtin et al. [14] to illustrate the role of coupling terms during mixed mode debonding. In Eqs. (8) and (9) we present an extension of the model to penalise overclosure ( $\Delta_n < 0$ ) when a compression of the interface is accompanied by a shear (tangential traction). This entails a removal of coupling terms from the expression for normal traction, i.e. if  $\Delta_n < 0$ ,  $T_n = T_n(\Delta_n)$ .

$$T_n(\Delta_n, \Delta_t) = \sigma_{max} \exp(1) \left( \frac{\Delta_n}{\delta_n} \right) \exp \left( -\sqrt{\frac{\Delta_n^2}{\delta_n^2} + \frac{\Delta_t^2}{\delta_t^2}} \right) \quad (6)$$

$$\Delta_n \geq 0$$

$$T_t(\Delta_n, \Delta_t) = \tau_{max} \exp(1) \left( \frac{\Delta_t}{\delta_t} \right) \exp \left( -\sqrt{\frac{\Delta_n^2}{\delta_n^2} + \frac{\Delta_t^2}{\delta_t^2}} \right) \quad (7)$$

$$T_n(\Delta_n) = \sigma_{max} \exp(1) \left( \frac{\Delta_n}{\delta_n} \right) \exp \left( -\sqrt{\frac{\Delta_n^2}{\delta_n^2}} \right) \quad (8)$$

$$\Delta_n < 0$$

$$T_t(\Delta_n, \Delta_t) = \tau_{max} \exp(1) \left( \frac{\Delta_t}{\delta_t} \right) \exp \left( -\sqrt{\frac{\Delta_t^2}{\delta_t^2}} \right) \quad (9)$$

$\sigma_{max}$  is the maximum normal traction (referred to hereafter as the “mode I interface strength”),  $\tau_{max}$  is the maximum tangential traction (referred to hereafter as the “mode II interface strength”).  $\delta_n$  and  $\delta_t$  are the normal and tangential interface characteristic lengths, respectively [13]. The cohesive zone model (CZM) is implemented through a user defined interface subroutine (UINTER).

The CF/PEEK material properties along with the calibrated material parameters for the damage and failure formulations previously described are listed in Table 1 below.

### 3. Micro-mechanical model of CF/PEEK micro-structure

Accumulations of micro-mechanical damage, such as fibre matrix debonding, can result in catastrophic failure of the laminate on a macro-scale. However, damage on a micro-scale is not predicted by the macro-scale analysis of the DRPs. Therefore, a micro-scale damage model is developed to gain an enhanced understanding of the micro-failure mechanisms of the composite fracture fixation plate under physiologically relevant loads. Micro-scale representative volume elements (RVE's) with fibre volume fractions (FVF) of 62% are constructed (a sample RVE is shown in Fig. 2(A)). A Python script is developed to implement a random sequential adsorption algorithm to randomly distribute the carbon fibres within the matrix. If a randomly generated fibre intersects the edge of the RVE another fibre is mirrored on the opposite face of the RVE to maintain periodicity. The RVE's used in this study have an overall size of  $50 \times 50 \mu\text{m}$  and a fibre diameter of  $5 \mu\text{m}$ .

Periodic boundary conditions [16] are applied along the boundaries of the RVEs to ensure that opposing faces remain parallel. The equations have been expressed in terms of nodal displacements vectors,  $\mathbf{u}$ , in Eqs. (10) and (11),

$$\mathbf{u}_a = \mathbf{u}_c - \mathbf{u}_{n4} \quad (10)$$

$$\mathbf{u}_d = \mathbf{u}_b - \mathbf{u}_{n2} \quad (11)$$

where, the subscripts  $a$ ,  $b$ ,  $c$  and  $d$  relate to nodes located on each face of the RVE and the subscripts  $n_2$ ,  $n_3$  and  $n_4$  correspond to the nodes located at the corners of the RVE, demonstrated in Fig. 2(Bi) and (Bii). The CZM model (Eqs. (6)–(9)) is used to simulate debonding of the matrix material from the embedded CFs. CZM characteristic lengths of  $1 \times 10^{-3} \mu\text{m}$  are applied at the fibre matrix interface [17,18]. Tensile tests are simulated on the micro-structural RVEs to calibrate the interface strength between individual fibres and the surrounding PEEK matrix. The normal and transverse interface strengths are assumed to be equal. Results are validated using experimental data for aligned  $90^\circ$  tension tests by Gallagher et al. [6]. Following calibration, the multi-axial strain state at the point of initial failure in a DRP is applied to the RVE to determine the microstructural failure mode under physiological loading. Table 2.

Neat PEEK material has been shown to exhibit asymmetric yielding, with a higher yield stress in compression than in tension. Furthermore, the plastic yielding of PEEK has been shown to be rate dependent in both tension and compression [20]. The strain sensitive extended Drucker–Prager model is used to simulate yielding of PEEK matrix material that surrounds the fibres in the micro-structural RVE model. The deviatoric stress measure is defined as:

$$t = \frac{q}{2} \left[ 1 + \frac{1}{K} - \left( 1 - \frac{1}{K} \right) \left( \frac{r}{q} \right)^3 \right] \quad (12)$$

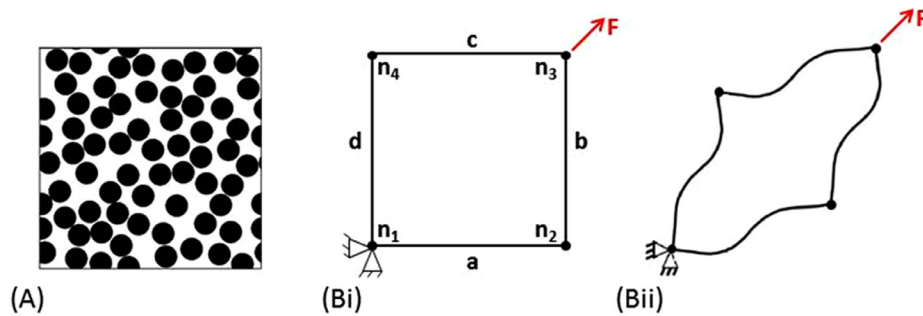


**Fig. 2.** (A) Illustration of the micro-mechanical representative volume elements with a 62% fibre volume fraction. (B) Schematic of the periodic boundary conditions applied to the RVE.

**Table 2**

Material properties of the PEEK matrix material and the embedded carbon fibres used in micro-mechanical simulations of RVE micro-structure.

Carbon fibre [19]	PEEK [2]
$E_{11} = 263$ GPa	$E = 4$ GPa
$E_{33} = E_{22} = 19$ GPa	$\nu = 0.36$
$\nu_{12} = \nu_{13} = 0.2$	$\sigma_{yt} = 108$ MPa
$\nu_{23} = 0.35$	$\sigma_{yc} = 142$ MPa
$G_{12} = G_{13} = 27.6$ GPa	
$G_{23} = 7.04$ GPa	

where  $K$  is the ratio of flow stress in triaxial tension to flow stress in triaxial compression,  $q$  is the Mises equivalent stress and  $r$  is the third invariant of deviatoric stress. This formulation allows for different yield values in tension and compression, as is the case with PEEK [20]. To ensure convexity of the yield surface  $0.778 \leq K \leq 1.0$ . The yield surface is defined as:

$$F = t - p \tan \beta - d = 0 \quad (13)$$

where  $p$  is the equivalent pressure stress ( $p = -\frac{1}{3}\text{trace}(\sigma)$ ),  $\beta$  is the friction angle of the material and  $d$  is the hardening parameter which measures the cohesion of the material. The linear form of the Drucker-Prager model for tri-axial compression is outlined below:

$$\sigma_1 - \sigma_3 + \frac{\tan \beta}{2 + \frac{1}{3}\tan \beta} (\sigma_1 + \sigma_3) - \frac{1 - \frac{1}{3}\tan \beta}{1 + \frac{1}{6}\tan \beta} \sigma_c^0 = 0 \quad (14)$$

The compressive and tensile yield strengths of unreinforced PEEK have been determined experimentally to be 108 MPa and 142 MPa, respectively [20]. Using these yield strength values returns values of  $\phi = 7.82^\circ$  and  $c = 61.9$  MPa for the friction angle and the matrix cohesion, respectively and the following Drucker-Prager parameters are calculated for PEEK  $K = 0.913$ ,  $\beta = 15.9^\circ$  and  $\sigma_c^0 = 141.96$  MPa.

## 4. Results

### 4.1. Macro-scale model of composite fracture fixation plate

Bending, torsion, and combined bending-torsion loading are applied to all laminated fixation plates. Failure loads and failure modes for each of the laminate layups are listed in Tables 3–5. A Factor of Safety (FoS) for each laminate is also computed based on published physiological loads (0.68 Nm torsion and 1.05 Nm bending moment).

Examining the computed FoSs listed in Table 3, it is clear that the laminate layup has a significant effect on the strength and failure location of the DRP in bending. The  $0^\circ$  laminate, whose fibres are aligned in the x-axis parallel to the axis of the radius bone,

has the highest predicted FoS in bending of 4.62. The  $0^\circ$  laminate is predicted to fail at an applied bending moment of 4.85 Nm. The  $90^\circ$  laminate, which has fibres aligned along the y-axis, provides very little resistance to the applied bending moment. An intra-laminar matrix crack is predicted to initiate at an applied bending moment of only 0.325 Nm (see Fig. 3(A)), more than ten times lower than the failure moment of the  $0^\circ$  laminate. The  $45^\circ$  laminate has a predicted FoS of 1.14, with the outermost plies predicted to fail due to a tensile matrix crack at an applied bending load of 1.2 Nm. The predicted mode of failure for the  $[\pm 45^\circ/0^\circ]_s$  laminate is intra-laminar tensile matrix cracking of the outermost  $45^\circ$  and  $-45^\circ$  plies (ply 1&2) at an applied bending moment of 3.51 Nm. The  $[0^\circ/\pm 45^\circ]_s$  laminate design is predicted to fail at an applied bending moment of 4.5 Nm. Similar to the  $0^\circ$  laminate, the predicted mode of failure is an intra-laminar matrix crack of the outermost ply at the edge of a screw hole.

All DRP designs fail at applied bending moments greater than physiological loads, apart from the  $90^\circ$  DRP. The  $[\pm 45^\circ/0^\circ]_s$  and  $[0^\circ/\pm 45^\circ]_s$  laminates have an equal number of  $0^\circ$  and  $\pm 45^\circ$  plies in their layup. However, a higher FoS is predicted for the  $[0^\circ/\pm 45^\circ]_s$  laminate. In the  $[\pm 45^\circ/0^\circ]_s$  laminate all the  $0^\circ$  plies are located near the centre of the DRP, whereas in the case of the  $[0^\circ/\pm 45^\circ]_s$  laminate the  $0^\circ$  plies are positioned on the outer surfaces of the DRP, thus providing a higher bending strength (28% greater than the  $[\pm 45^\circ/0^\circ]_s$  design).

As shown in Table 4, all DRP designs fail at applied torsional loads greater than physiological value ( $T_x = 0.68$  Nm). However, despite its high FoS in bending, the  $0^\circ$  laminate has the lowest FoS (1.37) in torsion, failing at an applied torque of 0.93 Nm, demonstrating that a design consisting of only  $0^\circ$  fibres does not provide a high resistance to torsional failure. In contrast, the predicted FoS of the  $90^\circ$  DRP in torsion is three times greater than the FoS predicted for the  $90^\circ$  plate in bending. A higher FoS for torsional loading is predicted for the  $45^\circ$  laminate design (FoS = 2.4). Failure occurs due to an intra-laminar matrix cracking parallel to the fibres in the first  $45^\circ$  ply at an applied torque of 1.63 Nm. Failure in the  $[\pm 45^\circ/0^\circ]_s$  DRP is predicted to occur due to intra-laminar matrix cracking in the outermost  $45^\circ$  plies at an applied torque of 1.78 Nm. The  $[0^\circ/\pm 45^\circ]_s$  DRP is predicted to fail due to an intra-laminar matrix crack at an applied torque of 1.22 Nm. The predicted torsional FoS for the  $[\pm 45^\circ/0^\circ]_s$  and the  $[0^\circ/\pm 45^\circ]_s$  laminates, 2.62 and 1.79, respectively, are lower than the corresponding values of FoS in bending (3.34 and 4.29, respectively).

DRP failure under combined bending/torsion loading is reported in Table 5. A ratio of applied bending moment to applied torque of  $M_y/T_x = 1.54$  is maintained throughout each simulation, based on physiologically measured values [8–10].

The highest FoS is computed for the  $[0^\circ/\pm 45^\circ]_s$  laminate (FoS = 2), followed by the  $[\pm 45^\circ/0^\circ]_s$  laminate (FoS = 1.72) are the only layups that will not fail within the allowable FoS under bending and torsional loading alone as well as under combined loading.



**Table 3**

Bending failure modes, applied moments at failure, and failure locations for all laminate layups.

Laminate layup	Mode of failure and location	Bending moment at failure (Nm)	Computed FoS
[0 <sub>8</sub> ]	Intra-laminar transverse tensile crack Ply 1 (0°) at a screw hole 9	4.85	4.62
[90 <sub>8</sub> ]	Intra-laminar transverse tensile crack Ply 1 (90°) (see Fig. 3(A))	0.325	0.31
[±45°]4s	Intra-laminar transverse tensile crack Ply 1 (45°) at a screw hole 8	1.20	1.14
[±45°/0°]4s	Intra-laminar transverse tensile crack Ply 1 (45°) at a screw hole 9	3.51	3.34
[0°/±45°]2s	Ply 2 (−45°) at edge of implant where distal end joins the main shaft Intra-laminar transverse tensile crack Ply 1 (0°) at a screw hole 9	4.5	4.29

**Table 4**

Torsional failure modes, applied torques at failure, and failure locations for all laminate layups.

Laminate layup	Mode of failure and location	Torsional moment at failure (Nm)	Computed FoS
[0 <sub>8</sub> ]	Intra-laminar transverse tensile crack Ply 16 (0°) at a screw hole 1	0.93	1.37
[90 <sub>8</sub> ]	Intra-laminar transverse tensile crack Ply 1 (90°) mid-line of main shaft of implant	0.97	1.43
[±45°]4s	Intra-laminar transverse tensile crack Plies 16 (45°), 14 (45°) and 2 (−45°) at laminate edge where main shaft meets hole 1	1.63	2.40
[±45°/0°]4s	Intra-laminar transverse tensile crack Plies 16 (45°), 15 (−45°), 14 (45°), 3 (45°) and 2 (−45°) at laminate edge (see Fig. 3(B))	1.78	2.62
[0°/±45°]2s	Intra-laminar transverse tensile crack Ply 16 (0°) at a screw hole 1	1.22	1.79

**Table 5**

Combined bending and torsion failure modes and failure locations for all laminate layups.

Laminate layup	Mode of failure and location	Combined moment at failure (Nm)	Computed FoS
[0 <sub>8</sub> ]	Intra-laminar transverse tensile crack Ply 16 (0°) at a screw hole 1	My = 1.50 Nm, Tx = 0.97 Nm	1.43
[90 <sub>8</sub> ]	Intra-laminar transverse tensile crack Ply 1 (90°) mid-line of main shaft of implant	My = 0.30 Nm, Tx = 0.19 Nm	0.29
[±45°]4s	Intra-laminar transverse tensile crack Ply 2 (−45°) at laminate edge	My = 1.34 Nm, Tx = 0.87 Nm	1.28
[±45°/0°]4s	Intra-laminar transverse tensile crack Ply 2 (−45°) at laminate edge (Fig. 4(A))	My = 1.81 Nm, Tx = 1.17 Nm	1.72
[0°/±45°]2s	Intra-laminar transverse tensile crack Plies 16 & 15 (0°) at hole 1 (Fig. 4(B))	My = 2.1 Nm, Tx = 1.36 Nm	2.0

In the case of the [±45°/0°]4s laminate, a crack is predicted in the outermost −45° ply (ply 2) at the laminate edge (Fig. 4(A)). In the case of the [0°/±45°]2s laminate, a crack is predicted in the outermost 0° plies (plies 16 and 15) at a screw hole (Fig. 4(B)).

The initial failure of each DRP design in bending, torsion and combined loading is computed to occur due to intra-laminar cracking. We next examine the required load to induce inter-ply delamination in the [0°/±45°]2s design. Fig. 5 shows the transverse stress distribution ( $\sigma_{22}$ ) in the [0°/±45°]2s laminate at applied loads of  $My = 4.58$  Nm,  $Tx = 2.96$  Nm (a factor of 4.4 times higher than physiological loading and 2.2 times higher than the load at initial intra-ply cracking). Significant levels of mode II delaminations are predicted in the shaft of the DRP around the first screw hole (highlighted in the insert). Under pure torsion the [0°/±45°]2s laminate undergoes mode II inter-ply delaminations at an applied load of 3.0 Nm, 2.5 times higher than the load at which intra-laminar cracking initiates. In the pure bending, inter-ply delamination is not predicted in the [0°/±45°]2s laminate at applied bending moments of 7.4 Nm, more than seven times greater than physiological loads.

A comparison of the stiffness and strength of the laminated DRP designs with a titanium implant of identical dimensions is shown in Fig. 6. All laminated DRP curves are plotted up to the point of intra-laminar cracking, whereas the curve for the titanium plate

is plotted up to the point at which the von Mises stress reaches the yield stress (825 MPa; see Table 1). As shown in Fig. 6(A), the bending stiffness of a laminated plate is highly dependent on the layup design. For example, the 0° and [0°/±45°]2s DRP exceed the bending stiffness of a titanium plate. In contrast, the bending stiffness of the [±45°/0°]4s DRP is ~50% of the titanium DRP. In torsion, all laminated DRP designs are significantly more compliant than the titanium DRP. In general, Fig. 6 illustrates the potential of laminated plate design to reduce stress shielding (associated with high stiffness metallic plates) while providing adequate strength to support physiological loading (see FoS values reported in Tables 3–5).

#### 4.2. Micro-scale model of fibre-matrix debonding in RVE

As indicated in Tables 3–5, intra-laminar tensile matrix cracking (Eq. (2)) is the initial failure mode of every single laminate DRP. While the layup design and the mode of loading strongly influences the crack location and FoS, for all prototype layup designs intra-laminar matrix cracking is predicted as the initial failure mode. The model parameters,  $Y_T$  and  $S$ , associated with this failure mode were calibrated and validated in a recent experimental-computational analysis of CF/PEEK. However, such macro-scale damage modelling does not uncover the precise failure mechanism

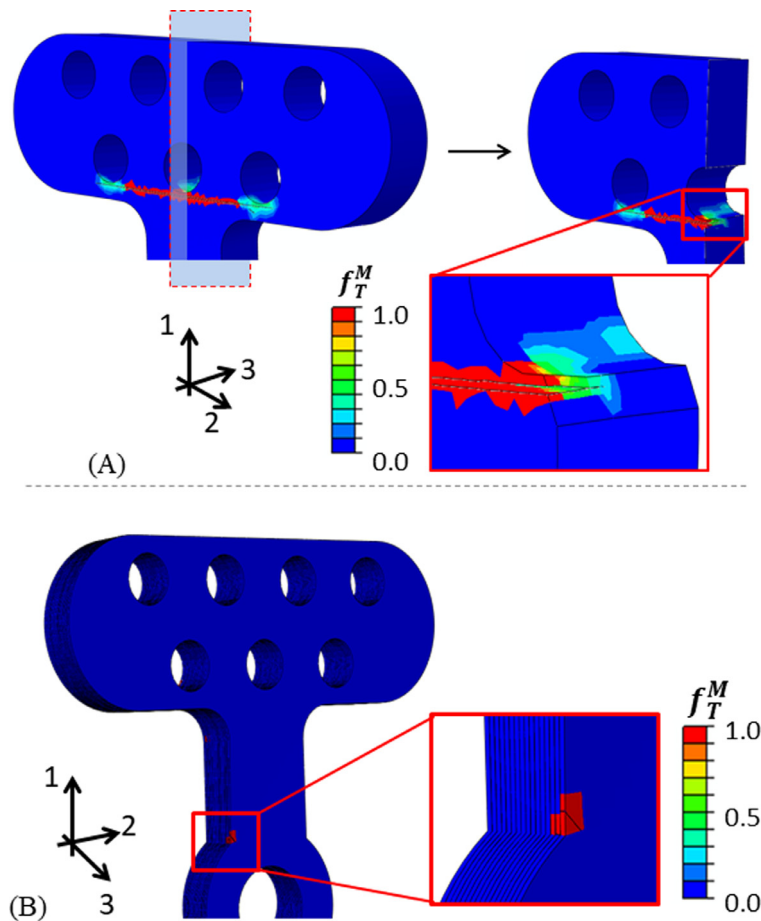


**Fig. 3.** (A) Computed crack propagation in the 90° laminated fixation plate at an applied bending moment of 1.4 Nm, where  $f_T^m$  is the tensile failure criterion (1.0 depicts an element that is fully cracked). (B) Computed crack propagation in the  $[\pm 45^\circ/0^\circ]_s$  laminated fixation plate at an applied torque of 1.78 Nm.

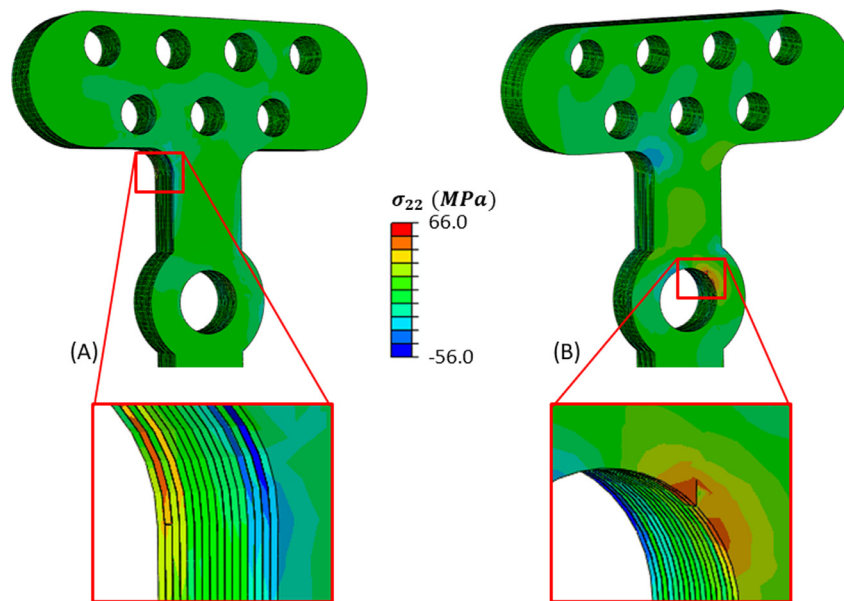


**Fig. 4.** Predicted intra-laminar transverse tension cracks under combined bending-torsion loading for: (A) the  $[\pm 45^\circ/0^\circ]_s$  DRP; and (B) the  $[0^\circ/\pm 45^\circ]_s$  DRP. Contours depict the distribution of transverse stress ( $\sigma_{22}$ ) for an applied load of  $M_y = 1.81$  Nm and  $T_x = 1.17$  Nm.

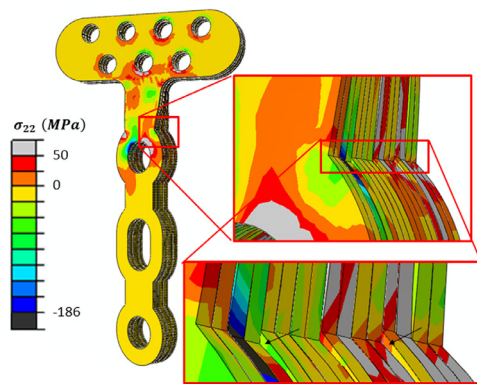


**Fig. 5.** Contour plot of the transverse stress ( $\sigma_{22}$ ) distribution in the  $[0^\circ_2/\pm 45^\circ]_{2s}$  laminate at the point of inter-laminar failure under combined loads of  $M_y = 4.58$  Nm,  $T_x = 2.96$  Nm, i.e. 4.4 times greater than physiological loading. Predicted mode II delamination is highlighted in the insert by black arrows.

that results in intra-laminar tensile matrix cracking. Here we perform a micro-mechanical analysis of a micro-structural RVE (as described in Section 3) to determine if intra-laminar tensile matrix cracking results from (i) ductile failure of the PEEK matrix, or (ii) localised debonding of the PEEK matrix from CFs.

#### 4.2.1. Micro-mechanical model calibration

The elastic plastic matrix material behaviour, including asymmetric yielding, has been experimentally characterised in a previous study [6] and Drucker–Prager material parameters are given in Section 3. However, the interface strength ( $\sigma_{max}$ ) between the matrix and the CFs has not previously been determined. Here we perform a parametric study to determine the interface strength, and consequently the failure mechanism, by comparing model predictions to experimental transverse tensile data from a previous study by the authors [6].

In Fig. 7(A) the predicted RVE stress-strain behaviour is compared to experimental data for a range of interface strengths. For a high interface strength ( $\sigma_{max} = 500$  MPa) matrix-fibre debonding is not computed. The stress-strain curve is stiffer than the experimental curve for strains greater than 0.001. A yield point is predicted at a stress of  $\sim 100$  MPa, followed by strain hardening. Such behaviour is not observed experimentally, specimen failure was observed at an ultimate strength of  $49.6 \pm 33.92$  MPa without any distinct yielding or strain hardening. An interface strength of  $\sigma_{max} = 110$  MPa results in the prediction of an ultimate strength of  $51.6 \pm 3.93$  MPa. Similar to experimental observation, the slope of the RVE stress-strain curve is predicted to reduce as a result

of progressive fibre-matrix debonding as the strain applied to the RVE is increased. Reduction of the interface strength to a value lower than 110 MPa results in an under-prediction of the ultimate strength of the RVE. Fig. 7(B) shows the predicted stress-strain curves and ultimate strength of five RVE geometries. Again, an interface strength of 110 MPa is used. Each RVE has a different randomly generated fibre distribution, with a fibre volume fraction of 62%. A reasonable match with experimental data is observed for all RVEs. A computed ultimate strength of  $51.6 \pm 3.93$  MPa at a strain of  $0.0058 \pm 0.0005$  is statistically similar ( $t(4) = -1.01$ ,  $p = 0.37$ ) to the experimental ultimate strength of  $49.6 \pm 3.92$  MPa at a measured strain of  $0.0054 \pm 0.0005$ . Fig. 7(C) shows that stress in the matrix material is reduced locally in region adjacent to a debonded surface. Fig. 7(D) shows the significant levels of fibre-matrix debonding at the point of failure of the RVE. Furthermore, Fig. 7(D) shows that the significant plastic deformation does not occur in the matrix during loading to failure. This further demonstrates that fibre-matrix debonding is the underlying failure mechanism in  $90^\circ$  tensile laminate tests, rather than plastic deformation or damage of the matrix material. In Fig. 7(E) the jagged nature of the fracture surface of a transverse tensile experimental specimen is shown. The discontinuous nature of the experimental crack shown is well described by the propagation of failure in the micro-mechanical RVEs.

#### 4.2.2. Micro-mechanical failure during macro-mechanical loading

We next use the micro-structural RVE to demonstrate that the failure mechanism of the laminated DRP is fibre-matrix debonding rather than plasticity or damage of the matrix material. Considering the  $[0^\circ_2/\pm 45^\circ]_{2s}$  laminated DRP, in Fig. 8(A) we show the strain state in the outermost  $0^\circ$  ply under physiological loading levels. Recall that our macro-scale damage model predicts cracking at point A in this ply when the applied loading is increased to twice the physiological level. At physiological loading (prior to the macro-scale prediction of cracking) the in-plane strain state orthogonal to the fibre direction at point A is computed as  $\gamma_{23} = 0.0024$ ,  $\varepsilon_{22} = 0.0025$  and  $\varepsilon_{33} = 0.0014$  (corresponding to in-plane principal strains of 0.00327 and 0.00063). This strain state is applied to the micro-mechanical RVE, and the resultant micro-structural stress distribution is shown in Fig. 8(Bi). No significant stress concentrations are observed in the matrix. Fig. 8(Bii) shows that at physiological loading no significant plastic deformation of the matrix or debonding is computed. The macro-scale damage model predicts cracking at Point A when applied loading is increased to twice the physiological level. The corresponding strain state ( $\gamma_{23} = 0.0048$ ,  $\varepsilon_{22} = 0.005$  and  $\varepsilon_{33} = 0.0028$ ) is applied to the RVE and the resultant micro-structural stress distribution is shown

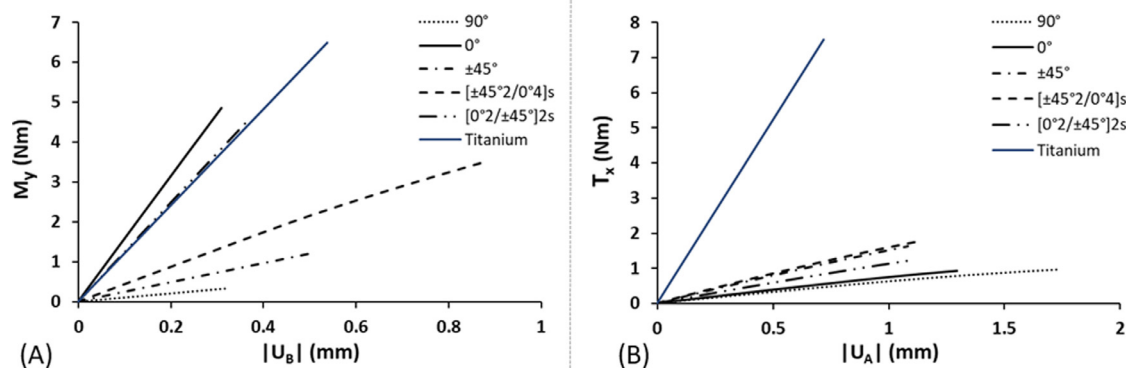


**Fig. 6.** (A) Applied bending moment versus deflection of Point B (see Fig. 1) for all laminate layups and for titanium DRP. (B) Applied torque versus deflection of Point A (see Fig. 1) for all laminate layups and for titanium DRP. Curves are plotted up to the point of failure. Failure for the titanium plate is characterised by the onset of plastic deformation.

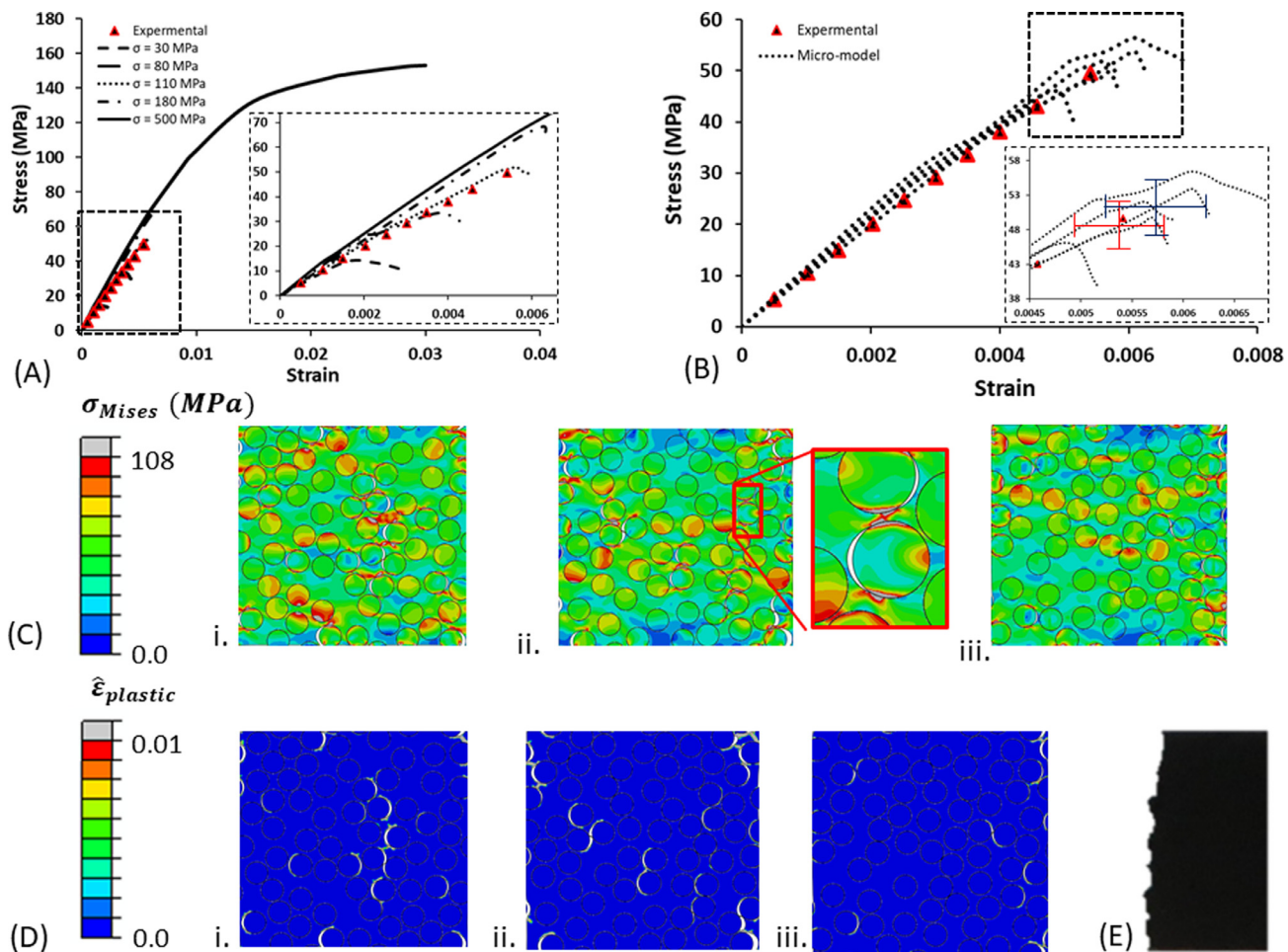


**Fig. 7.** (A) Computed RVE nominal stress-nominal strain curves for a range of interface strengths ( $\sigma_{max}$ ) for a single RVE geometry subjected to uniaxial tensile loading. Experimental uniaxial transverse tensile stress-strain curve [6] used to calibrate  $\sigma_{max}$ . (B) Nominal stress-nominal strain uniaxial tension curves for five RVE geometries with interface strengths of  $\sigma_{max} = 110$  MPa. Insert shows the mean and standard deviations of failure stress and failure strain for experimental data [6] (red crosshairs) and the RVE predictions (navy crosshairs). (C) Contour plots of the equivalent plastic strain ( $\epsilon_{pl}$ ) distribution in three separate RVEs at the point of failure under uniaxial tension. (D) Contour plots of the von Mises stress ( $\sigma$ ) distribution in the RVEs at the point of failure under uniaxial tension. (E) Experimental image of crack propagation through 90° laminate from experiments carried out by Gallagher et al. [6].

in Fig. 8(Ci). While significant stress concentrations are computed, the matrix stress is relaxed adjacent to debonded surfaces. Significant levels of fibre-matrix debonding are computed, with 18 of the 76 fibres (24%) partially separating from the matrix. Highly localised plastic deformation of the PEEK matrix is computed in locations of stress concentrations. While higher areas of plastic deformation computed for this multi-axial loading than for uniaxial tensile loading (Fig. 7(D)), the levels of plastic deformation in Fig. 8(Cii) are not sufficiently high (maximum  $\epsilon_{pl} = 0.05$ ) to result in ductile failure of the matrix material [20], and fibre-matrix debonding is again the micro-structural failure mechanism.

## 5. Discussion

The current study demonstrates that CF/PEEK laminated DRPs can be designed with similar geometric dimensions to conventional metal plates while providing sufficient structural strength to support physiological levels of loading. Macro-scale structural analysis of a distal radius fracture fixation plate highlights the importance of ply orientation. A high number of 0° plies near the outer surfaces results in a greater bending strength while the addition of 45° plies increases the torsional strength of the laminates. Ply layout design significantly influences the effective bending stiffness of the DRP. [0°/±45°]2s and 0° laminates exceed the

effective bending stiffness of titanium DRP, whereas a [±45°/0°]s laminate provides a bending stiffness that is ~50% that of a titanium DRP. All laminate designs provide an effective torsional stiffness that is significantly lower than that of a titanium DRP. However, it should be noted that the torsional stiffness of long bones is significantly lower than the bending stiffness; experiments carried out on adult femurs report a torsional stiffness of 5.0 Nm/deg, compared to a bending stiffness of 2.5 GPa [21]. The demonstrated potential of laminated DRPs to provide reduced bending and torsional stiffness, while still providing sufficient strength to support physiological loading, can be exploited to eliminate stress shielding associated with traditional metallic implants [22]. While the current study does not determine an optimal device configuration, the detailed analysis of five ply layout configurations provides, for the first time, an outline of the key challenges and benefits of developing CF/PEEK laminated orthopaedic implants.

Macro-scale DRP simulations incorporate a multi-axial multi-mode damage model calibrated and validated in a recent experimental-computational study by the authors. This macro-scale damage model incorporates intra-laminar cracking, interlaminar delamination, and anisotropic plasticity. Implementation of this multi-mode damage framework for the simulation of DRPs under physiological loading predicts that intra-laminar transverse tensile crack is the primary mode of DRP failure under physiological



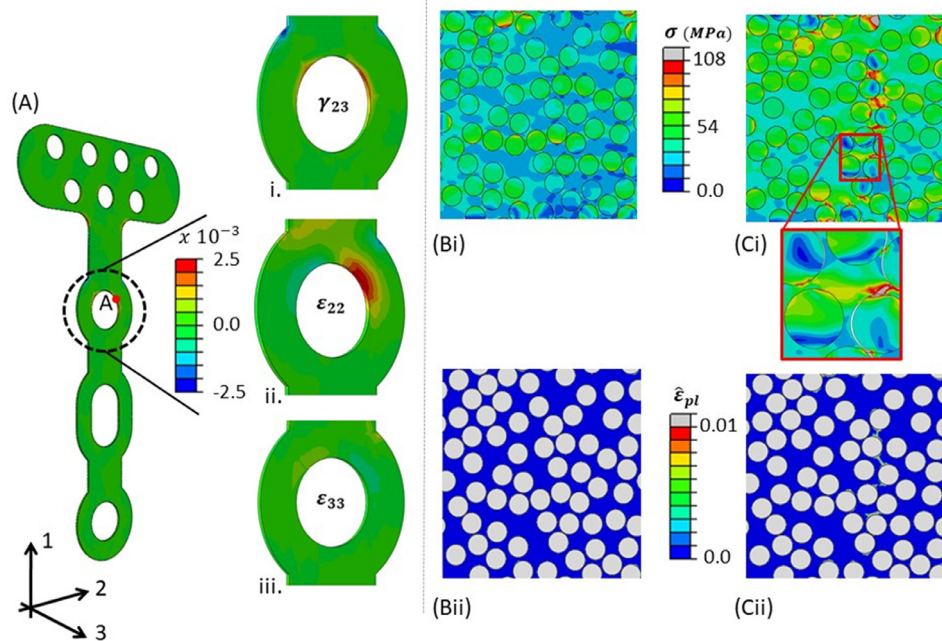


**Fig. 8.** (A) Multi-axial strain state at Point A in the outermost ply of the  $[0_2/\pm 45]_2s$  laminated DRP under physiological loading ( $M_y = 1.05$  Nm,  $T_x = 0.68$  Nm). Computed strain-state is applied to micro-structural RVE. (B) Von Mises stress ( $\sigma$ ) and equivalent plastic strain ( $\epsilon_{pl}$ ) distributions in RVE at physiological loading. (C) Von Mises stress ( $\sigma$ ) and equivalent plastic strain ( $\epsilon_{pl}$ ) distributions in RVE at two times physiological loading. Inserts highlight matrix-fibre debonding. Macro-model predicts transverse tensile cracking at Point A at this level of applied loading.

loading. We perform a multi-scale micro-mechanical analysis of the CF-PEEK microstructure to uncover the precise mechanism under-lying intra-laminar transverse tensile crack. Simulations reveal that this damage mechanism results from debonding of the PEEK matrix from CF fibres. Plastic strains in the matrix material are not sufficiently high to result in ductile failure of the matrix. The fibre-matrix interface strength of Optima UR is computed to be 110 MPa. Reported experimental values for the fibre matrix interface strength of carbon fibre reinforced polymers have been as high as 202 MPa [23]. Fibre sizing, a process by which a film is dispersed onto the surface of the fibre in order to improve the surface chemistry, could be considered to increase the fibre-matrix adhesion [24,25]. However to date, PEEK remains largely incompatible with most sizings, due to their low degradation temperatures ( $\sim 250^\circ\text{C}$ ), to overcome this new high performance thermoplastic sizing formulations are being developed [26].

The current study implements a rigid fixation of screws to the CF/PEEK implant and to the bone fragments. A previous experimental and computational investigation examined the influence of osteon orientation on the bone-screw pull-out strength [27]. Using such techniques, a follow-on study is currently being performed to characterise the pull-out strength at the screw-laminate interface. Future investigations should also consider fretting fatigue damage at the screw-laminate interface using established experimental and computational techniques [28,29]. The current modelling framework can also be readily used to investigate the response of implants to a range of loading rates. Further studies should assess the influence of stiffness and anisotropy of CF/PEEK substrates on cell behaviour [30–32], in addition to investigation of CF/PEEK debonding and cracking on cell adhesion [33,34]. Furthermore, the effect of altered peri-prosthetic strain rate on osteoblast biomechanical behaviour following device implantation should be investigated [35,36].

Through careful selection of the orientation of individual plies, the macro-scale effective anisotropy composite fracture plates can be matched to the anisotropic properties of bone, which is itself a self-assembling aligned long fibre reinforced composite material.

Therefore, different laminate configurations can be designed for different areas in the body, as a function of both the physiological loading conditions and the density and anisotropy of the peri-prosthetic bone. Careful laminate design can also limit the stress concentrations near screw holes, minimizing the possibility of screw pull out. This is critically important if CF/PEEK laminates are to provide a clinically viable alternative to metal fixation plates. Laminate failure around the screw hole will be examined in greater detail in a follow-on experimental and computational study.

## Funding

This work was supported by funding from the [Irish Research Council \[GOIPG/2013/735\]](#).

## Conflicts of interest

None.

## Ethical approval

Not required.

## Acknowledgments

Access to computational resources was provided by the Irish Centre for High-End Computing (ICHEC).

## Supplementary materials

Supplementary material associated with this article can be found, in the online version, at doi:[10.1016/j.medengphy.2019.03.006](https://doi.org/10.1016/j.medengphy.2019.03.006).

## Appendix A

In “Abaqus/Standard” implicit finite element schemes contact mechanics entails the definition of a master and a slave surface.

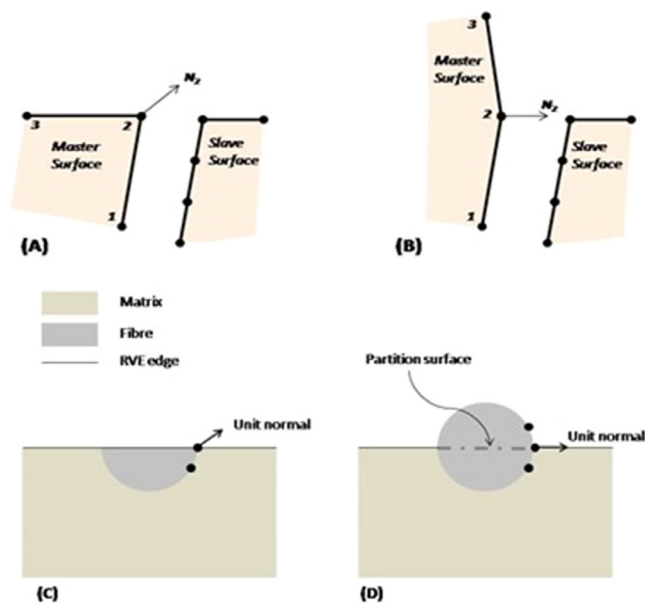


**Fig. A1.** Schematic of the unit normal vector calculated for node 2 on two master surface geometries (A) and (B); illustration of the unit normal calculated for the corner node of a fibre crossing the boundary of the RVE for (C) a sectioned fibre and (D) a partitioned fibre.

Under finite-deformation large-sliding conditions and any given slave node may interact with any subset of master surface nodes. The subset of master surface nodes is identified by defining the nearest neighbour nodes to the point on the master surface closest to the slave node. Before defining this nodal subset, unit normal vectors for each node on the master surface must be computed. The unit normal vector is calculated by averaging the unit normal vectors of the two segments either side of a given node. As an example, an interaction between master surface nodes (labelled 1, 2 and 3) and a slave surface is shown in Fig. A1(A) and (B): the unit normal vector of node 2 is calculated by averaging the unit normal vectors of segments 1–2 and 2–3.

Examining Fig. A1(A) and (C), it is clear that if a fibre crossing the boundary of the RVE is sectioned along the boundary edge, a skewed unit normal vector will be calculated. As a result of the skewed unit normal vector numerical singularities occur on the corner nodes of the sectioned fibres. However, if the fibre is left whole, demonstrated in Fig. A1(B) and (D), the correct normal vector is calculated. For this study the fibres crossing the borders of the RVE have not been sectioned but partitioned in line with the edge of the RVE, leaving a “dummy portion” of the fibre on the outside of the RVE. Such “dummy portions” do not provide any structural contribution to the model but are merely used to define correct normal vectors for contact calculations at the face of the RVE. The periodic boundary conditions are applied along the fibre partition so that the periodic deformation of the RVE is correctly implemented.

## References

- [1] Rohner B, Wieling R, Magerl F, Schneider E, Steiner A. Performance of a composite flow moulded carbon fibre reinforced osteosynthesis plate. *Vet Comp Orthop Traumatol* 2005;18:175–82.
- [2] Kurtz SM, Devine JN. PEEK biomaterials in trauma, orthopedic, and spinal implants. *Biomaterials* 2007;28:4845–69. doi:10.1016/j.biomaterials.2007.07.013.
- [3] Tarallo L, Mugnai R, Adani R, Zambianchi F, Catani F. A new volar plate made of carbon-fiber-reinforced polyetheretherketon for distal radius fracture: analysis of 40 cases. *J Orthop Traumatol* 2014;15:277–83. doi:10.1007/s10195-014-0311-1.
- [4] Rhee PC, Shin AY. The rate of successful four-corner arthrodesis with a locking, dorsal circular polyether-ether-ketone (PEEK-Optima) plate. *J Hand Surg Eur Vol* 2013;38:767–73. doi:10.1177/1753193413475962.

- [5] Steinberg EL, Rath E, Shlaifer A, Chechik O, Maman E, Salai M. Carbon fiber reinforced PEEK Optima-A composite material biomechanical properties and wear/debris characteristics of CF-PEEK composites for orthopedic trauma implants. *J Mech Behav Biomed Mater* 2012;17:221–8. doi:10.1016/j.jmbbm.2012.09.013.
- [6] Gallagher EA, Lamorinière S, McGarry P. Multi-axial damage and failure of medical grade carbon fibre reinforced PEEK laminates: experimental testing and computational modelling. *J Mech Behav Biomed Mater* 2018;82:154–67. doi:10.1016/j.jmbbm.2018.03.015.
- [7] Osada D, Viegas SF, Shah MA, Morris RP, Patterson RM. Comparison of different distal radius dorsal and volar fracture fixation plates: a biomechanical study. *J Hand Surg Am* 2003;28:94–104. doi:10.1053/jhsu.2003.50016.
- [8] Christen P, Ito K, Knippels I, Müller R, van Lenthe GH, van Rietbergen B. Subject-specific bone loading estimation in the human distal radius. *J Biomech* 2013;46:759–66. doi:10.1016/j.jbiomech.2012.11.016.
- [9] Gordon KD, Kedgley AE, Ferreira LM, King GJW, Johnson JA. Design and implementation of an instrumented ulnar head prosthesis to measure loads in vitro. *J Biomech* 2006;39:1335–41. doi:10.1016/j.jbiomech.2005.03.002.
- [10] Hirahara H, Neale PG, Lin Y-T, Cooney WP, An KN. Kinematic and torque-related effects of dorsally angulated distal radius fractures and the distal radial ulnar joint. *J Hand Surg Am* 2003;28:614–21. doi:10.1016/S0363-5023(03)00249-1.
- [11] Hill R. A theory of the yielding and plastic flow of anisotropic metals. *Proc R Soc A Math Phys Eng Sci* 1948;193:281–97. doi:10.1098/rspa.1948.0045.
- [12] Feerick EM, Liu XC, McGarry P. Anisotropic mode-dependent damage of cortical bone using the extended finite element method (XFEM). *J Mech Behav Biomed Mater* 2013;20:77–89. doi:10.1016/j.jmbbm.2012.12.004.
- [13] McGarry JP, Ó Máirtín É, Parry G, Beltz GE. Potential-based and non-potential-based cohesive zone formulations under mixed-mode separation and over-closure. Part I: theoretical analysis. *J Mech Phys Solids* 2014;63:336–62. doi:10.1016/j.jmps.2013.08.020.
- [14] Ó Máirtín É, Parry G, Beltz GE, McGarry JP. Potential-based and non-potential-based cohesive zone formulations under mixed-mode separation and over-closure Part II: finite element applications. *J Mech Phys Solids* 2014;63:363–85. doi:10.1016/j.jmps.2013.08.019.
- [15] Niinomi M. Mechanical properties of biomedical titanium alloys. *Mater Sci Eng A* 1998;243:231–6. doi:10.1016/S0921-5093(97)00806-X.
- [16] Dowling EP, Ronan W, McGarry JP. Computational investigation of in situ chondrocyte deformation and actin cytoskeleton remodelling under physiological loading. *Acta Biomater* 2013;9:5943–55. doi:10.1016/j.actbio.2012.12.021.
- [17] O'Dwyer D, O'Dowd N, McCarthy C. Numerical micromechanical investigation of interfacial strength parameters in a carbon fibre composite material. *J Compos Mater* 2013;48:749–60. doi:10.1177/0021998313477172.
- [18] Cooper R, Chyung K. Structure and chemistry of fibre-matrix interfaces in silicon carbide fibre-reinforced glass-ceramic composites: an electron microscopy study. *J Mater Sci* 1987;22.
- [19] Banerjee S, Sankar BV. Mechanical properties of hybrid composites using finite element method based micromechanics. *Compos Part B Eng* 2014;58:318–27. doi:10.1016/j.compositesb.2013.10.065.
- [20] Rae PJ, Brown EN, Orlor EB. The mechanical properties of poly(ether-ether-ketone) (PEEK) with emphasis on the large compressive strain response. *Polymer (Guildf)* 2007;48:598–615. doi:10.1016/j.polymer.2006.11.032.
- [21] Cristofolini L, Viceconti M, Cappello A, Toni A. Mechanical validation of whole bone composite femur models. *J Biomech* 1996;29:525–35. doi:10.1016/0021-9290(95)00084-4.
- [22] Ganesh VK, Ramakrishna K, Ghista DN. Biomechanics of bone-fracture fixation by stiffness-graded plates in comparison with stainless-steel plates. *Biomed Eng Online* 2005;4. doi:10.1186/1475-925X-4-46.
- [23] Sarasua J, Remiro P, Pouyet J. The mechanical behaviour of PEEK short fibre composites. *J Mater Sci* 1995;30:3501–8.
- [24] Blacketter DM, Upadhyaya D, King TR, King JA. Evaluation of fiber surfaces treatment and sizing on the shear and transverse tensile strengths of carbon fiber-reinforced thermoset and thermoplastic matrix composites. *Polym Compos* 1993;14:430–6. doi:10.1002/pc.750140510.
- [25] Wu Q, Li M, Gu Y, Wang S, Yao L, Zhang Z. Effect of sizing on interfacial adhesion of commercial high strength carbon fiber-reinforced resin composites. *Polym Compos* 2016;37:254–61. doi:10.1002/pc.23176.
- [26] Giraud I, Franceschi S, Perez E, Lacabanne C, Dantras E. Influence of new thermoplastic sizing agents on the mechanical behavior of poly(ether ketone)/carbon fiber composites. *J Appl Polym Sci* 2015. doi:10.1002/app.42550.
- [27] Feerick EM, McGarry JP. Cortical bone failure mechanisms during screw pull-out. *J Biomech* 2012;45:1666–72. doi:10.1016/j.jbiomech.2012.03.023.
- [28] McCarthy OJ, McGarry JP, Leen SB. Microstructure-sensitive prediction and experimental validation of fretting fatigue. *Wear* 2013. doi:10.1016/j.wear.2013.05.012.
- [29] McCarthy OJ, McGarry JP, Leen SB. Micro-mechanical modelling of fretting fatigue crack initiation and wear in Ti–6Al–4V. *Int J Fatigue* 2014. doi:10.1016/j.ijfatigue.2013.04.019.
- [30] Ronan W, Deshpande VS, McMeeking RM, McGarry JP. Cellular contractility and substrate elasticity: a numerical investigation of the actin cytoskeleton and cell adhesion. *Biomech Model Mechanobiol* 2014. doi:10.1007/s10237-013-0506-z.
- [31] McGarry JP. Characterization of cell mechanical properties by computational modeling of parallel plate compression. *Ann Biomed Eng* 2009. doi:10.1007/s10439-009-9772-4.

- [32] McEvoy E, Deshpande VS, McGarry P. Free energy analysis of cell spreading. *J Mech Behav Biomed Mater* 2017. doi:[10.1016/j.jmbbm.2017.06.006](https://doi.org/10.1016/j.jmbbm.2017.06.006).
- [33] McGarry JP, McHugh PE. Modelling of in vitro chondrocyte detachment. *J Mech Phys Solids* 2008. doi:[10.1016/j.jmps.2007.08.001](https://doi.org/10.1016/j.jmps.2007.08.001).
- [34] Reynolds NH, Ronan W, Dowling EP, Owens P, McMeeking RM, McGarry JP. On the role of the actin cytoskeleton and nucleus in the biomechanical response of spread cells. *Biomaterials* 2014. doi:[10.1016/j.biomaterials.2014.01.056](https://doi.org/10.1016/j.biomaterials.2014.01.056).
- [35] Weafer PP, Reynolds NH, Jarvis SP, McGarry JP. Single cell active force generation under dynamic loading Part I: AFM experiments. *Acta Biomater* 2015. doi:[10.1016/j.actbio.2015.09.006](https://doi.org/10.1016/j.actbio.2015.09.006).
- [36] Reynolds NH, McGarry JP. Single cell active force generation under dynamic loading Part II: Active modelling insights. *Acta Biomater* 2015. doi:[10.1016/j.actbio.2015.09.004](https://doi.org/10.1016/j.actbio.2015.09.004).